PHYSICAL REVIEW C **78**, 064609 (2008)

Attosecond time delays in heavy-ion induced fission measured by crystal blocking

J. U. Andersen and J. Chevallier
Department of Physics, University of Aarhus, DK-8000 Aarhus C, Denmark

J. S. Forster
Département de Physique, Université de Montréal, Québec, H3C 3J7 Canada

S. A. Karamian
FLNR, Joint Institute for Nuclear Research, RU-141980 Dubna, Russian Federation

C. R. Vane, J. R. Beene, A. Galindo-Uribarri, J. Gomez del Campo, C. J. Gross, H. F. Krause, E. Padilla-Rodal, D. Radford, and D. Shapira
Oak Ridge National Laboratory, Oak Ridge, Tennessee 37831, USA

C. Broude
Physics Department, Weizmann Institute of Science, Rehovot, Israel

F. Malaguti and A. Uguzzoni
Department of Physics, University of Bologna and I.N.F.N., I-40126 Bologna, Italy
(Received 7 August 2008; published 18 December 2008)

The time delays in fission induced by bombardment of W with 180 MeV ^{32}S, 240–255 MeV ^{48}Ti, 330–375 MeV ^{58}Ni, and 390 MeV ^{74}Ge have been measured by observation of crystal blocking. Nearly all results are consistent with exponential decay with lifetimes of order 10^{-18} s which depend weakly on the atomic number of the composite nucleus. This is inconsistent with the Bohr-Wheeler model of fission from a compound nucleus in statistical equilibrium at each stage in a neutron evaporation cascade and supports a picture of strongly damped quasifission. A simple diffusion model with one-body dissipation reproduces roughly the observed time scale and the exponential decay. It suggests that the outer fission barrier could play a significant role in the observed, very slow decays.

DOI: 10.1103/PhysRevC.78.064609 PACS number(s): 24.75.+i, 25.70.Jj, 25.70.Lm, 61.85.+p

I. INTRODUCTION

We have carried out measurements by crystal blocking of time delays in nuclear fission induced by heavy-ion bombardment. Crystal blocking is a time-of-flight technique in which charged particles emitted in nuclear decay at a lattice site are blocked by a row of atoms, leading to a dip in yield in the direction of a crystal axis. The dip is reduced if, due to the recoil in the reaction, the decaying nucleus is displaced from the row by more than about 5 pm [1]. With increasing displacement in the range 5–100 pm the dip becomes narrower and shallower, and it vanishes for larger displacements. With recoil velocities of a few times 10^6m/s, lifetimes of attoseconds can be measured (1 as = 10^{-18} s). The shape of the dip reveals whether a filling-in is due to a well defined delay, giving a recoil displacement in the range of sensitivity, or to the tail of a broad time distribution. Such a tail gives a component with no blocking and hence an increase in minimum yield but no narrowing of the dip.

Fission induced by light ions was studied by crystal blocking in the 1970s, and the measurements revealed a tail in the time distribution stretching to times longer than 10^{-16} s [2–7]. This could be understood from the Bohr-Wheeler model of a compound nucleus (CN) in statistical equilibrium as an intermediate stage in the fusion-fission process [8]. Fission competes mainly with evaporation of neutrons, and after each neutron emission the nuclear temperature is reduced and the lifetime for fission is strongly increased. When the fission yield has contributions from several stages in this cascade ('multichance fission'), the time scale for fission can therefore span many orders of magnitude. A simple case with only fast first-chance and slow second-chance fission of uranium was studied in detail with crystal blocking [9]. The crystal-blocking results for fission induced by bombardment with light ions were shown to be consistent with statistical-model calculations of multichance fission, which also reproduced the independently measured average numbers of neutrons emitted before fission [6].

However, later measurements with direct information on time delays have yielded surprisingly long delays for fission of nuclei with high excitation energy and fairly low fission barrier. For such nuclei fission should dominate over neutron emission and a time scale much shorter than attoseconds is expected for early-chance fission, with a very small probability of late-chance fission. An experiment in the early 1990s on fission of highly excited uranium nuclei showed that an appreciable fraction of the fission events were slower than the atomic K-vacancy lifetime of 7 as [10], and this result was corroborated by crystal blocking measurements [11,12]. Even more surprising were recent observations of similar long delay times for fission of superheavy nuclei with atomic number near 120, created in heavy-ion collisions [13,14]. The results were interpreted as stability of a compound nucleus with a fairly high fission barrier due to shell effects, but this is difficult to reconcile with observations of very low cross sections for formation of evaporation residues (ER) of superheavy nuclei [15]. (See the discussion in [16].)

Fairly long fission times have also been deduced from observations of neutron emission and giant-dipole gamma rays. Systematic measurements of fission induced by high-energy heavy ions have shown that many neutrons are emitted prior to fission even for nuclei with a fission barrier so low that the fission yield should be dominated by first-chance fission. The physical explanation is thought to be highly viscous flow of nuclear matter which delays equilibration of the fission degree of freedom in the compound nucleus and slows down the descent from saddle to scission. Typically, an initial time delay is introduced in the analysis, during which neutron emission but not fission is possible, and in the subsequent statistical decay with competition between the two decay channels, the fission width is reduced to account for diffusion back-flow at the saddle. Total average fission times of a few times 10^{-20} s have been deduced from the neutron emission [17,18] and slightly longer delays from emission of giant-dipole-resonance gamma rays [19]. Although long on the nuclear time scale, these times are much shorter than those observed with the more direct techniques.

The indirect lifetime techniques clearly tell something about the lifetime of the fissioning nucleus but there are problems with the quantitative interpretation of this message. The pre-scission neutron number is a highly nonlinear clock since at the end of the evaporation cascade the neutron lifetime may increase by an order of magnitude or more after each evaporation. Therefore, even small errors in the average neutron number have a large influence on the deduced lifetime, and different measurements are not always consistent [20,21]. In addition, the interpretation is model dependent. Fission times longer by an order of magnitude have been deduced from an alternative analysis of the same data for neutron emission [22]. Here the reactions were treated as mainly quasifission, i.e., fission without formation of a compound nucleus, and the calculated lifetimes are longer mainly because there is then less excitation energy available for neutron emission than in the compound nucleus.

With the aim of providing more direct information on the lifetimes, we have carried out crystal blocking experiments with beams of ^{32}S, ^{48}Ti, ^{58}Ni, and ^{74}Ge ions inducing fission in a thin W crystal. The composite nuclei have atomic numbers ranging from $Z = 90$ to $Z = 106$. According to theory [23], these reactions are in a transition region where the reaction mechanism changes from mainly compound-nucleus fission to quasifission without CN formation. As mentioned below, there is recent experimental evidence for dominance of quasifission even for ^{32}S bombardment.

Measurements with 170–180 MeV ^{32}S beams (performed at the tandem accelerator at the University of Munich, Garching by a group wich included some of the present authors) have been previously reported [24]. Now we have extended the measurements to 240–255 MeV ^{48}Ti, 330–375 MeV ^{58}Ni, and 390 MeV ^{74}Ge beams. The analysis of the early data for ^{32}S beams [24] did not reveal any fission delays. However, in a preliminary publication of a small selection of the present data we applied a more sophisticated analysis and found strong effects of fission delay, even for ^{32}S bombardment. Lifetimes of order 2 as were deduced [25]. The key to the interpretation was an analysis of the shape of the blocking dips, with a comparison between the blocking of fission fragments and of elastically scattered ions which took into account an angular smearing due to mosaic structure of the thin target crystals. Much effort has since been spent on tests of the calibration and of the analysis, and we have found a significant correction to the angular calibration of our detector, which reduces somewhat the difference between blocking dips for fission and for elastic scattering.

Except for the ^{32}S induced fission, the blocking results are well reproduced with an exponential distribution of delay times with a single value of the lifetime. This is strong evidence for the failure of the picture of multichance fission of a Bohr compound nucleus. The measured lifetimes are of order 1 as (somewhat shorter than reported earlier due to the calibration correction). This is much longer than obtained by the conventional analysis of neutron measurements [17,18]. However, when differences in excitation energy are taken into account, the results may be consistent with the alternative analysis of neutron measurements in [22].

It is important for a qualitative interpretation of experiments on heavy-ion induced fission and also, in some cases, for quantitative analysis of the experiments to know whether or not the fission proceeds via compound nucleus formation. For reactions between very heavy ions, the probability for CN formation is small. The reason is that the initial configuration with two touching nuclei is less compact than the shape of the compound nucleus at the fission barrier, and there is an energy barrier depending on the asymmetry in the collision, which hinders the complete fusion (see, for example, Fig. 7 in [16]). Recently, experimental evidence has been obtained, indicating that except for fission induced by very light ions (e.g., ^{12}C and ^{16}O), the probability for CN formation in heavy-ion reactions is small [26–28].

With the possible exception of ^{32}S + W, the reactions we have studied should lead mainly to quasifission without CN formation. This is supported by our observation of a single lifetime since there is then no competition between fission and neutron emission, leading to a broad time distribution. However, a picture of heavy-ion induced fission as quasifission with lifetimes of attoseconds is quite surprising. An alternative name for quasifission is 'fast fission' and, indeed, early studies of correlations between scattering angles and mass distributions in quasi-fission indicated lifetimes of only a few times 10^{-21} s [29]. Since there is no large fission barrier to overcome in quasifission, the explanation for the long delay must be sought in strong damping of the deformation dynamics. The question is then, whether the observed very long lifetimes can be explained on the basis of current theoretical understanding of nuclear dynamics.[1]

[1]The estimates of fission times were developed in discussions of our results with W. J. Swiatecki.

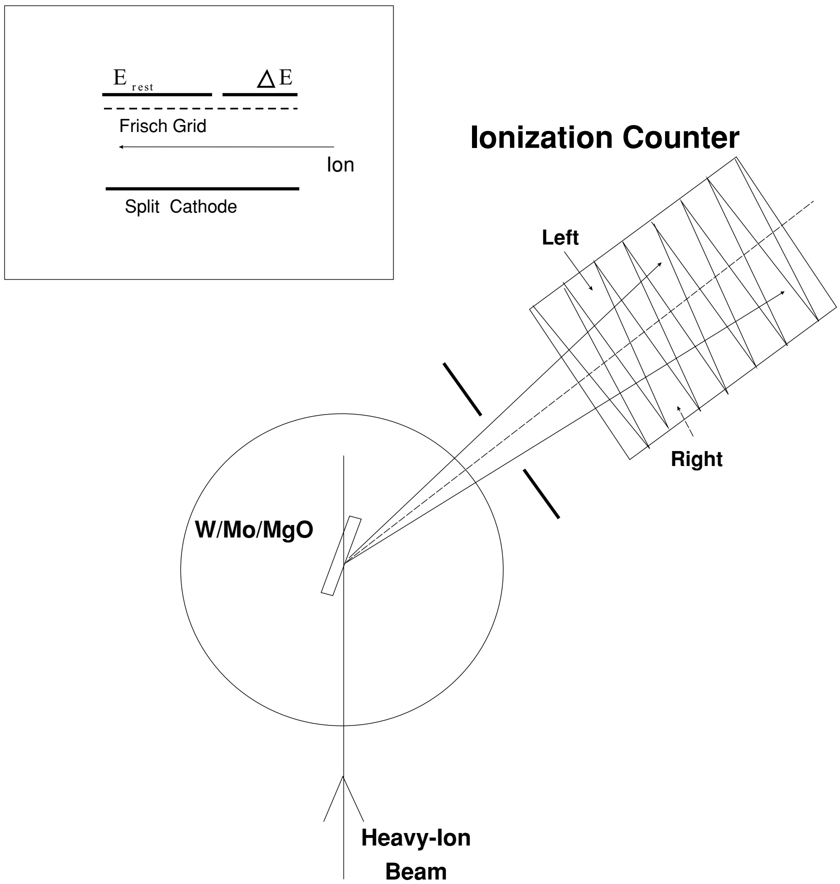

FIG. 1. Experimental layout.

An important observation is that for the collision systems studied here, the liquid drop potential surface for the composite system has a very flat region. This was also noted in [21, 22], where it was pointed out that the driving force for the deformation is so weak that the dynamics must be described by a stochastic equation. In the analysis in [22] no attempt was made to give a theoretical estimate of the time delay associated with this stochastic evolution and the time delay was instead derived semi-empirically from a calculation of the statistical neutron emission during the fission process and a fit to measured numbers of pre-scission neutrons.

A way to estimate the delay time theoretically is indicated by recent work on cross sections for ER formation in heavy-ion collisions producing superheavy nuclei [16,30,31]. The small probabilities for CN formation were here estimated from a simple calculation of diffusion in a parabolic potential representing a barrier for fusion, and the results reproduced measurements rather well. We apply the same diffusion equation with standard one-body dissipation and show that the simplest estimates indeed lead to diffusion times of order 1 as for a stochastic development from the merging of the two nuclei to a configuration close to scission. We also estimate the influence on the diffusion time of a possible shallow potential minimum, deriving from a combination of the liquid drop energy and the shell effects, which give rise to a secondary minimum near the 2:1 deformation ratio [32].

II. EXPERIMENTAL DETAILS

The measurements were carried out at the Holifield Radioactive Ion Beam Facility (HRIBF) with stable beams from the 25 MV tandem. Data were collected in three separate experiments. Fission and elastic scattering was measured with ion beams of ^{48}Ti at energies of 240, 245, and 255 MeV in the first experiment and ^{58}Ni at 330, 350, and 375 MeV in the second experiment. In the third experiment beams of ^{32}S ions at 55 and 180 MeV, ^{58}Ni ions at 111 and 350 MeV, and ^{74}Ge ions at 219, 299, and 390 MeV were used.

The blocking measurements were made with 75 nm thick crystals of natural W grown on a 200 nm thick crystal of Mo, which, in turn, was grown on an MgO substrate with a ⟨100⟩ axis normal to its surface; for the third experiment the W crystal was 50 nm thick. The crystal was oriented with a ⟨111⟩ axis (at 35.3° to the crystal surface) pointing at the center of the detector positioned at 54.3° to the beam, with the result that the beam was incident at 19.0° to the target surface. The beam was collimated by two apertures 1.75 mm in diameter positioned 27.6 and 101.3 cm ahead of the crystal. For the second experiment the collimator closest to the crystal was 1 mm in diameter.

Elastically scattered ions and reaction products were detected in a large-solid-angle ionization counter with an entrance aperture of 8 cm by 8 cm at 56.2 cm from the target [33]. The pressure of the CF_4 gas in the counter was

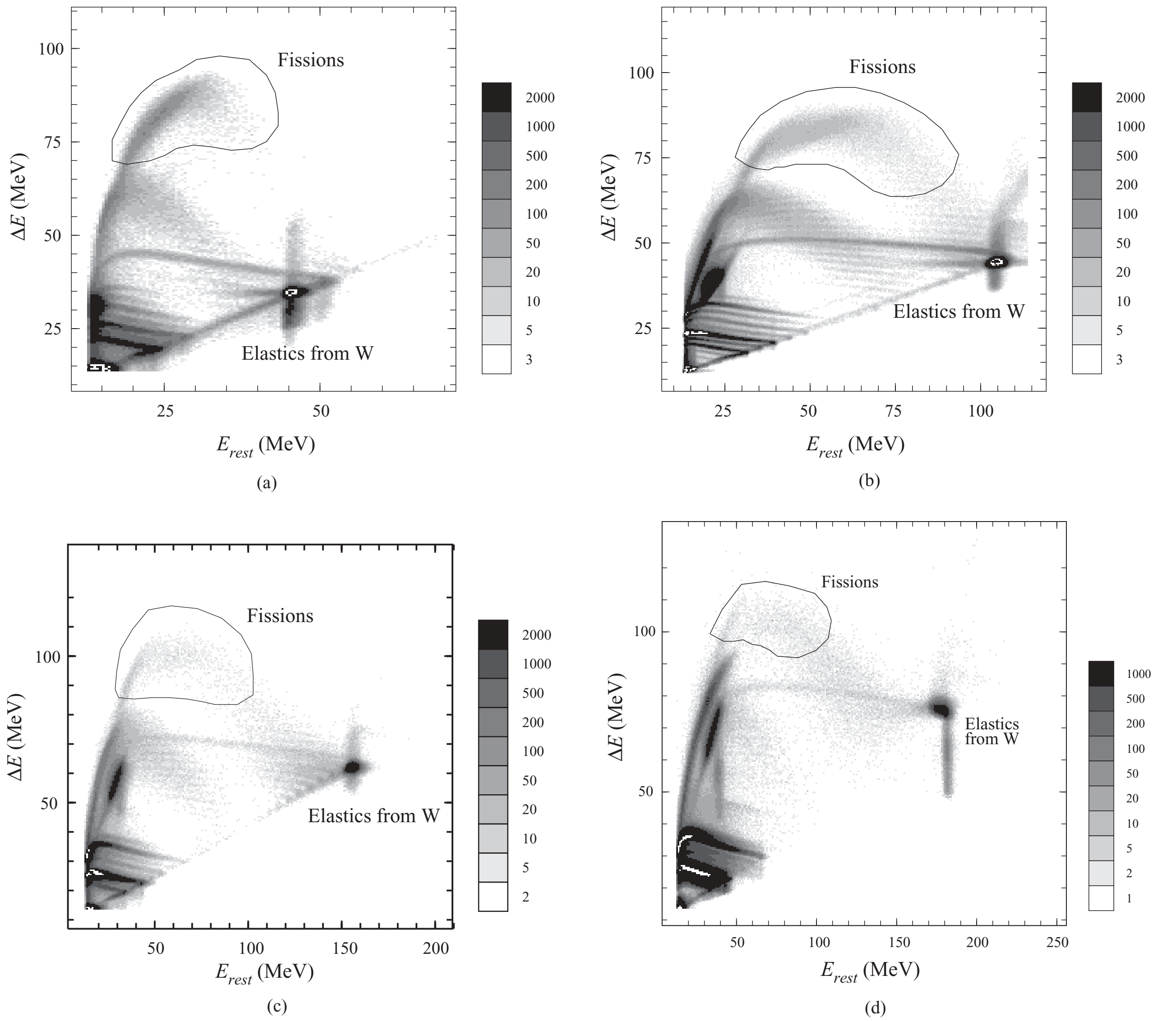

FIG. 2. Two-dimensional spectra obtained with the gas counter for (a) 180 MeV ^{32}S, (b) 245 MeV ^{48}Ti, (c) 350 MeV ^{58}Ni (third experiment), and (d) 390 MeV ^{74}Ge. The polygons used to define fission events are indicated.

adjusted to stop fission fragments (35 Torr). To ensure that particles entering the counter did not strike the electrodes or the sides of the counter an aperture of 3.8 cm by 3.8 cm was placed 36.2 cm from the target resulting in a solid angle of 11 msr and an acceptance angle of ±3 degrees in x and in y about the center of the aperture.

A schematic layout of the experimental setup is shown in Fig. 1. In the inset at the top the counter is seen from the side and the ions are incident from the right. The anode of the counter is split into two electrodes, and the first (12 cm long) gives a ΔE signal. The second electrode (18 cm long) gives an E_{rest} signal and the total energy deposited in the counter is the sum $\Delta E + E_{\mathrm{rest}}$. Only events with a signal in both sections of the counter were accepted. The detector has the capability to determine the average (x, y) position of the particle path in the counter. The x sensitivity is achieved with a cathode electrode in the shape of a backgammon, as indicated in the figure. The zigzag line separates a left and a right electrode, and an x signal is obtained from the signals from the left (l) and right (r) sections as the ratio $(l - r)/(l + r)$. Since the signal from the cathode is dependent on the distance of the trajectory of the detected particle from the cathode (the closer to the cathode the bigger the signal) a y signal is obtained from the ratio of the cathode and anode signals, i.e., as $(l + r)/(\Delta E + E_{\mathrm{rest}})$. The x and y coordinates of the particle at the entrance are then determined from the x and y signals through a nonlinear transformation using calibration data taken through a mask, as described below.

The split anode provides a means of particle identification from a plot of ΔE vs E_{rest}, as shown in Fig. 2 for the four beams used in this work. The region of the plot corresponding to fission fragments is marked. The light particles appearing as nearly horizontal lines in the lower part of the plot come mainly from reactions within the thick substrate. The ions scattered elastically from W appear as a small circle because of the small energy loss in the thin target. Since the gas pressure is low

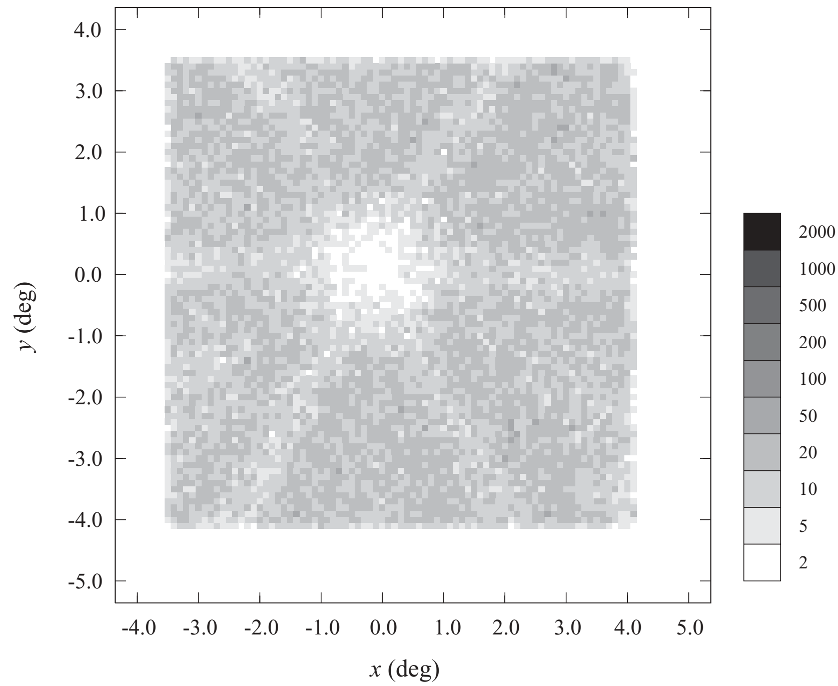

FIG. 3. Blocking pattern along a ⟨111⟩ axial direction for fission fragments from 245 MeV ^{48}Ti bombardment of a thin W crystal.

the highest energy light reaction products such as elastically scattered ions do not stop in the detector, and there is a folding back of these lines in the ΔE vs $E_{\rm rest}$ plot. At the left hand side of the plot there are two ridges of counts with a positive slope of ΔE vs $E_{\rm rest}$. These contain signals from recoiling Mo and W atoms, the W signals being concentrated in a spot due to the small thickness of the W crystal.

The event-by-event data consisting of ΔE, $E_{\rm rest}$, l, and r were recorded on the data acquisition computer for later playback.

III. DATA ANALYSIS

The event-by-event data were played back with selection of events inside polygons set on the fission and elastic regions in the ΔE vs $E_{\rm rest}$ plot. For events in the fission and elastic polygons, a two-dimensional (2D) plot of the x and y signals was generated with the equations given above. The x and y coordinates at the entrance to the counter were obtained from a non-linear transformation based on a set of data for elastic scattering of the beam through a calibration mask placed in front of the detector. The mask has a 9 by 9 array of 1.0 mm diameter holes at 5.0 mm spacing and was placed 41.6 cm from the target. The transformation was derived from the requirement that the centroids of the "peaks" in the mask x-y spectra transform into a square grid. This procedure also provides an angular calibration of the detector. Mask data were collected for beams of 240 MeV ^{48}Ti, 330 MeV ^{58}Ni, 111 MeV ^{58}Ni, 350 MeV ^{58}Ni, 55 MeV ^{32}S, 180 MeV ^{32}S, and 219 MeV ^{74}Ge.

The mask data were collected only for elastically scattered ions but the calibration transformation was applied also to fission fragments after some corrections. In our previous work [24], we observed that the y signal depends on the mass of the detected particle, and we scaled the y-coordinate for the fissions so that the axis of the fission and elastic blocking patterns occurred at the same y-coordinate. In the first analysis of the present data [25], we refined this correction and introduced a linear dependence of this y-scaling on the parameter $E_{\rm rest}$, ensuring that the coordinates of the center of the blocking dip were the same for all fission fragments as those for the elastics.

In the comprehensive analysis of the data presented here we have obtained a better understanding of this correction and discovered that also the angular scale must be corrected for fission fragments. The origin is easily understood from the schematic drawing of the setup in Fig. 1. The x and y signals depend on an average over the length of the counter of the x and y distances from the center line at which the particle energy is deposited as ionization. For a given angle of the trajectory, the signals therefore depend on the range of the particle. Since fission fragments have a shorter range than the elastically scattered particles used for the mask calibration, this dependence leads to a systematic underestimate of the angles for fission fragments. The effect was clearly visible in a comparison of the 2D plots of the x and y signals for fission and for elastic scattering. These plots are images of the 3.8 by 3.8 cm entrance aperture in front of the counter, and the limits of the image were larger in both the x and y directions for elastic scattering. We have scaled the x and y signals so that the limits of the aperture image for fission were equal to the limits for elastic scattering. The corrections were linear in the fraction of energy lost in the $E_{\rm rest}$ portion of the counter, $E_{\rm rest}/(\Delta E + E_{\rm rest})$. They were derived with the further condition that they should vanish for the values of $E_{\rm rest}$ and ΔE for elastically scattered ions. They resulted in a 5–10% "stretching" of the fission pattern in x and y about the position of the axis.

A corrected 2D x vs y plot for fissions from 245 MeV ^{48}Ti bombardment of W is shown in Fig. 3. The experimental blocking dips shown in the following figures were obtained from circular averages about the blocking minimum in the two-dimensional spectra. As pointed out earlier [6] this has

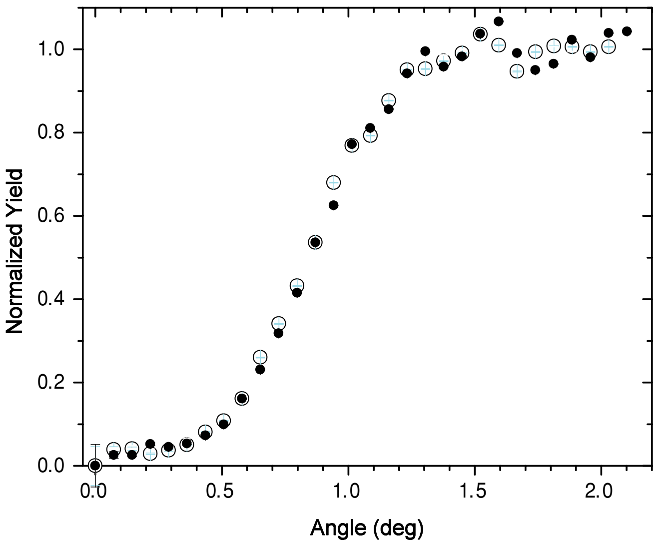

FIG. 4. (Color online) Axial blocking dip for elastic scattering of 111 MeV ^{58}Ni, (○) with calibration using mask data recorded at 111 MeV and (●) with calibration for fissions using mask data recorded at 350 MeV.

the advantage of improving statistical accuracy as well as eliminating the influence of planar blocking effects which is clearly seen in Fig. 3.

To test the correction procedure we compared the 2D blocking patterns for 55 MeV ^{32}S and 111 MeV ^{58}Ni data, generated using the mask data taken with the same beam, with the blocking patterns generated using the mask data taken at the higher energy and applying the same corrections as for fissions. The agreement is excellent, as illustrated for the Ni case in Fig. 4. The fraction of the energy lost in the E_{rest} part of the counter is even smaller for elastic scattering at 111 MeV than for fission, so this gives us confidence in the accuracy of the correction procedure.

The lower energy beams, 55 MeV ^{32}S, 111 MeV ^{58}Ni, 219 and 299 MeV ^{74}Ge, all stopped in the active part of the detector giving us a means to calibrate the energy response of the detector. In addition we have used W recoils from the high energy ^{74}Ge beam. A problem in the calibration is the energy loss in the target and in the 1 μm mylar foil at the entrance to the counter (up to about 10 MeV) which, for a given energy, depends on the atomic number and mass of the particle. We have solved this problem approximately by performing a linear calibration with W recoils as representative of the heavier fission fragments and the 219 and 299 MeV ^{74}Ge elastically scattered ions as representative of the lighter and more energetic fission fragments.

IV. CALCULATION OF BLOCKING DIPS

In our analysis we have used the simplest description of the blocking of charged particles by rows of atoms along a crystal axis, the continuum approximation. We give below the few formulas from the Lindhard theory on which the calculations are based [34]. In the comparisons with experiments, the measured yield is averaged over the azimuthal angle for fixed angle of the beam to the axis. This elimination of the perturbations caused by the arrangement of the atomic rows in crystal planes is for thin crystals justified by Lindhard's rule of angular averages applied to planar blocking.

The small angle scattering of the particle by the atoms is described as motion in a potential, $U(\vec{r})$, which is the average along the axis of the particle-crystal Coulomb interaction at a position $\vec{r}$ in the plane perpendicular to the axis ("transverse plane"). For a particle with energy E moving at an angle ψ to the axis, the so-called transverse energy, $\varepsilon = E\psi^2 + U(\vec{r})$, is then conserved along the trajectory. We have added the potentials from the six nearest rows using Lindhard's standard potential for a single row, corrected for thermal vibrations,

$$U_s(r) = E\psi_1^2 \left\{ \frac{1}{2} \ln\left(\frac{3a^2}{r^2 + u_1^2} + 1 \right) \right\}, \tag{4.1}$$

expressed in terms of the characteristic blocking angle,

$$\psi_1 = \left(\frac{2Z_1 Z_2 e^2}{Ed} \right)^{1/2}. \tag{4.2}$$

Here Z_1 and Z_2 are the atomic numbers of the particle and the crystal atoms, d is the spacing of atoms in the rows along the axis, and the length a is the Thomas-Fermi screening distance, $a = 0.8853\, Z_2^{-1/3} a_0 = 11$ pm. The square of the one-dimensional vibrational amplitude, u_1^2, in the denominator is a simplified correction for thermal vibrations, giving the correct maximum potential. For tungsten at room temperature the amplitude is $u_1 = 5$ pm.

We make the further assumption that when the particles reach the crystal surface the flux is uniform in transverse phase space at fixed transverse energy ε (statistical equilibrium). For two-dimensional motion this implies that the flux is also uniform within the available area. At an angle ψ_e to the axis outside the crystal, the modification by crystal blocking of the flux of particles emitted at the transverse position $\vec{r}_e$ inside the crystal is then given by

$$Y\left(\vec{r}_e, E\psi_e^2\right) = \int_{A_0} d^2\vec{r} \int_{\varepsilon > U(\vec{r}_e)} d\varepsilon \frac{1}{A(\varepsilon)} \delta\left(\varepsilon - E\psi_e^2 - U(\vec{r})\right). \tag{4.3}$$

Here A_0 is the unit cell area in the transverse plane and $A(\varepsilon)$ is the area accessible to a particle of transverse energy ε. The outer integral is over points of exit from the crystal and the delta function picks out the transverse energy contributing to the flux at angle ψ_e. If $\vec{r}_e$ is close to a row, the potential $U(\vec{r}_e)$ is high. At small angles, ψ_e, the function Y is then much smaller than unity because the outer integral only has contributions from the small region with $U(\vec{r}) \geqslant U(\vec{r}_e)$. This is the crystal blocking effect.

The modification of the total emitted flux is obtained by integration over the distribution, $P(\vec{r}_e)$, of emission points,

$$Y_{\mathrm{tot}}\left(E\psi_e^2\right) = \int d^2\vec{r}_e P(\vec{r}_e) Y\left(\vec{r}_e, E\psi_e^2\right). \tag{4.4}$$

For elastic scattering, the distribution $P(\vec{r}_e)$ is centered at a row, with a Gaussian broadening from thermal vibrations. For fission there is in addition a displacement due to the delay t of the emission, given by vt, where v is the projection of the recoil velocity on the transverse plane.

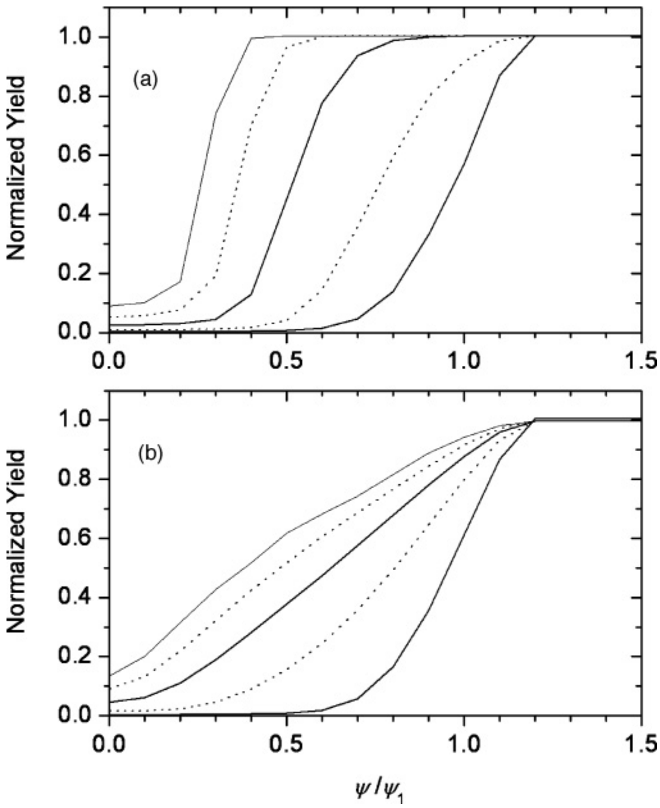

FIG. 5. Continuum model calculations of blocking dips for different displacements of the emitting nucleus from a ⟨111⟩ row of W atoms, with (a) fixed displacements and (b) exponential distributions of displacements. The (mean) displacement varies from 0 to 40 pm in steps of 10 pm.

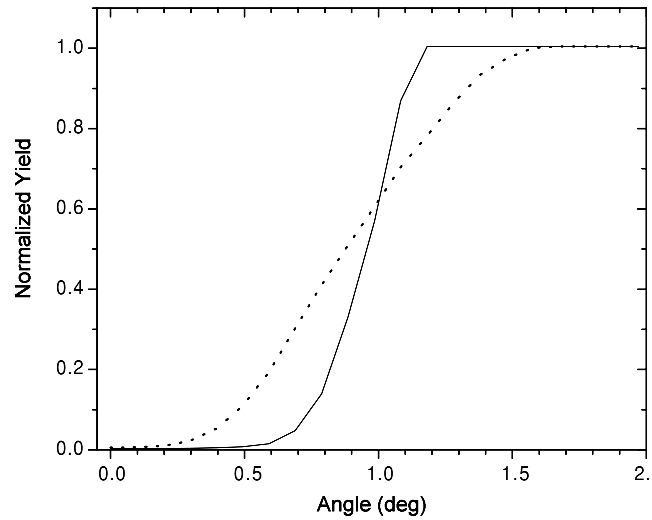

FIG. 6. Illustration of the influence of neutron recoil. The parameters correspond to fission induced by 180 MeV ^{32}S and isotropic emission of a 1 MeV neutron by a fragment after it has moved away from the atomic row containing the emitting atom. Full line no neutron, dashed line one neutron.

The calculations are illustrated in Fig. 5 by blocking dips for a series of displacements. In Fig. 5(a) the displacements are well defined. For zero displacement the width is close to the Lindhard angle in Eq. (4.2), and the main effect of the displacements on the blocking dip is a strong narrowing as the displacement increases. For the exponential distributions of displacements, corresponding to exponential decays, there is a stronger increase of the yield in the bottom of the dip, associated with the tail of large displacements, but a narrow dip remains because the recoil is chosen to be parallel with a plane so that the recoiling atom is moving towards a neighboring row [6].

A different recoil effect, which could disturb the interpretation of measurements, is the change of the blocking dip due to emission of a neutron from the fission fragment. The effect of a 1-MeV neutron emitted isotropically from a fission fragment after the blocking by scattering on nearby row atoms is illustrated in Fig. 6. If the neutron is emitted before this scattering the recoil has no effect on the blocking. Since most neutrons are emitted at times much shorter than the time required for the fragment to pass a few row atoms, which is of order 10^{-16} s, the effect is therefore expected to be small.

To test the accuracy of the continuum approximation, we have compared it with Monte Carlo simulations for a W crystal of about 130 nm, corresponding to the thickness of our targets along the blocking axis [35]. The dips for zero and 15 pm displacements are compared in Fig. 7(a). For zero displacement, corresponding to blocking of elastically scattered particles, there is a deviation in the shoulder region just outside the dip but the overall agreement is quite good. For the narrower dip the agreement is nearly perfect. In Fig. 7(b) the two types of calculation are compared for an exponential distribution of displacements, corresponding to exponential decay by fission. Also here the overall agreement is very good but the yield at small angles is higher by a factor of about 1.5 in the simulation, the so-called Barrett factor. Both this enhancement and the shoulder depletion in Fig. 7(a) are well known effects due to the influence of crystal planes on the axial blocking pattern [36–39].

The calculations in Fig. 7 were carried out with the Lindhard potential. It is known to be a little too strong but we have found that the blocking dip for elastic scattering is only slightly narrower (5%) when calculated with the more accurate Molière potential. Both potentials use the Thomas-Fermi screening distance a as a parameter. With the value given above we include only screening by target electrons. The screening by projectile electrons depends on the projectile velocity. At low velocities the atomic projectile carries nearly all its electrons and they should give a significant contribution to the screening. Lindhard suggested an effective screening distance obtained by the replacement $Z_2^{-1/3} \rightarrow (Z_1^{2/3} + Z_2^{2/3})^{-1/2}$ in the formula for a, but at high velocities the projectile carries few electrons and their contribution to the screening is strongly reduced. We can estimate the influence on the blocking dip from the formula for the half width in the continuum approximation with the Lindhard potential for a single row [34],

$$\psi_{1/2} = \psi_1 \left[\frac{1}{2} \ln\left(\frac{(Ca)^2}{2u_1^2 \ln 2} + 1\right)\right]^{1/2}. \tag{4.5}$$

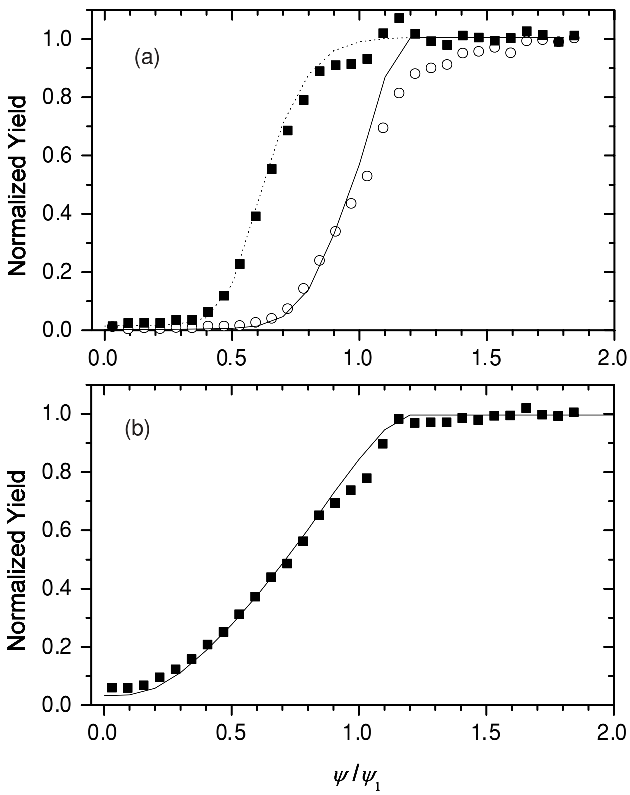

FIG. 7. Comparison of continuum model calculations (curves) with Monte Carlo simulations for (a) fixed displacements of 0 (full line) and 15 pm (dashed) and (b) an exponential distribution with average value 15 pm. Fission fragments were emitted isotropically with angles less than 2.9 deg to the axis, at ten depths from 6.6 nm to 125 nm. The Lindhard angle is $\psi_1 = 0.9$ deg.

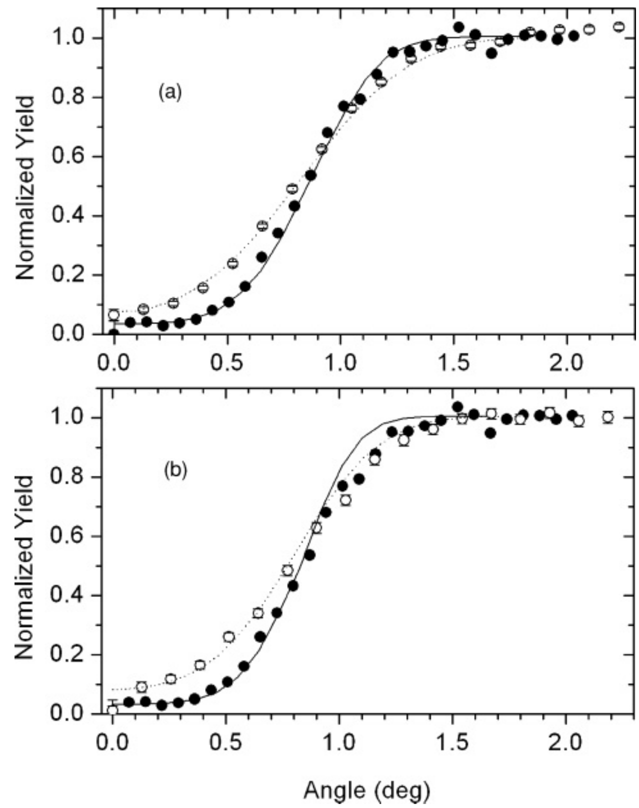

FIG. 8. Illustration of the effect of mosaic structure on the energy scaling of blocking dips, for elastic scattering of (a) 55 MeV (●) and 180 MeV (○) ^{32}S and (b) 111 MeV (●) and 350 MeV (○) ^{58}Ni. The angles are for the higher energies scaled by the square root of the energy ratio. The curves are continuum model calculations including a Gaussian mosaic spread of 0.35 deg FWHM.

As shown below, we have measured blocking for elastic scattering of projectiles with Z_1 varying from 16 to 32 and found no indication of a violation of the simple scaling of the halfwidth with ψ_1. With the Lindhard prescription for a, the change in $\psi_{1/2}/\psi_1$ should have been 3%, with a further change by 3% for a variation of Z_1 from 32 to 54. We have used the screening distance for tungsten in all calculations, without a correction for projectile screening.

In this description, the width of the blocking dip scales with the angle ψ_1 in Eq. (4.2). For fission fragments there is a distribution in energy and atomic number and hence in the parameter ψ_1. In calculations of fission blocking the first correction is an average over this distribution.

Next there are corrections for the imperfect experimental conditions. First, the finite size of the beam spot gives a smearing of the dip. The diameter of the beam was about 2 mm and due to the tilt of the crystal the beam spot on the target was elongated in the horizontal plane. As seen along the $\langle 111\rangle$ axis, at 35.3° to the surface, the elongation is $\sin(35.3°)/\sin(19°) = 1.77$. A corresponding angular smearing was introduced in the calculations.

There is a similar but much larger correction for mosaic structure of the thin W crystals. It is a well-known property of thin epitaxially grown W crystals that they consist of small crystallites with a spread in orientation of a few tenths of a degree [40]. This is most important at high energy where the blocking dip is narrow, and we have determined the mosaic spread from measurements of blocking dips for elastic scattering at different energies. This is illustrated in Fig. 8 by elastic scattering of S and Ni beams. The data at the higher energies were recorded together with a blocking dip for fission fragments, and the lower energies were chosen to give about the same value of ψ_1 as for these fission fragments. The high-energy dips have been scaled in angle by the square root of the ratio of the energies so that the dips should be identical if the scaling with ψ_1 were perfect. The large discrepancy is mainly due to the mosaic spread, and the dips are well reproduced by a convolution of the calculated dip with a Gaussian angular distribution of the direction of the $\langle 111\rangle$ axis, with FWHM = 0.35°.

Finally, there is a small correction for disorder in the crystal, mainly at the interfaces. In Fig. 8, the 'random' fraction of the crystal has in both cases been assumed to be 3%, corresponding to an amorphous layer of about 2 nm. This correction just raises the minimum yield by 3% without affecting the width of the dip.

We have also measured elastic scattering for Ge at several energies and the blocking dip for scattering of 219 MeV Ge is shown in Fig. 9. The agreement with the calculation is good and the measured dip even seems slightly broader than the calculated one, indicating that the scaling with ψ_1 is not

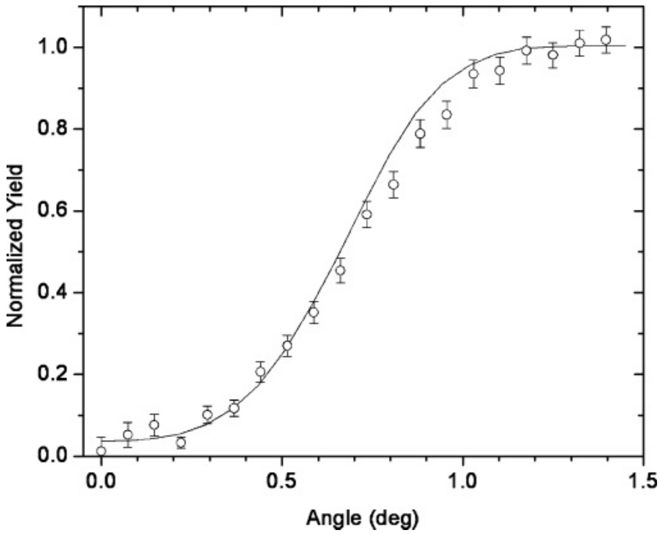

FIG. 9. ⟨111⟩ blocking dip for elastic scattering of 219 MeV ^{74}Ge compared with continuum model calculation.

significantly affected by projectile-electron screening, which would lead to a narrowing. The lowering of the shoulder region by multiple scattering is seen also in Figs. 7(a) and 8.

V. PRESENTATION OF DATA

An important element in the identification of fission fragments with the gas counter is a comparison of the energy spectra with theoretical predictions. This is illustrated for three cases in Fig. 10. The events are selected by the polygons in the 2D-plots in Fig. 2, and the spectra are compared with calculations based on the mean fission energies from [41] and a Gaussian mass distribution. The agreement is good for the central region with cut-offs at low and high energies, more abrupt at low energies due to the polygon shape. For Ti the energy spectra are very similar at the other bombarding energies. The Ni measurement is from the third experiment with the thinner crystal. A narrower polygon was used for the other Ni data and also for the Ge measurement, where the separation from deep inelastic scattering is less well-defined. The average energies of the selected fragments are given in Table I.

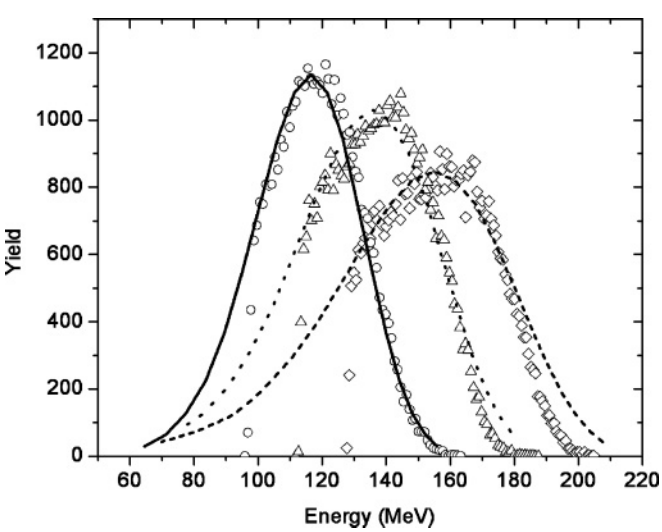

FIG. 10. Fission energy spectra corresponding to the polygons in Figs. 2(a)–2(c), 350 MeV ^{58}Ni (◇), 245 MeV ^{48}Ti (Δ), and 180 MeV ^{32}S (○). The curves are calculations with Gaussian fragment-mass distributions and the average kinetic energies from [41].

For the calculation of blocking dips, both the distributions in energy and in atomic number of the fragments are needed. We have assumed a fixed charge-to-mass ratio for the fragments in a given reaction and have calculated the relation between energy, E, and atomic number, Z, from the fission kinematics. In the 2D-plots in Fig. 2, the spread in ΔE for fixed E reveals a spread in Z for given mass, M, but the relative spread in E (and M) is much larger. As seen in Fig. 2(c), the Z values can be identified as nearly horizontal lines for inelastic scattering just left of the elastic scattering peak. We have extrapolated the linear relation between Z and ΔE into the high-energy edge of the fission polygon and found good agreement with the calculated relation between Z and E. This supports our analysis but it is not a very stringent test.

The blocking dips for 180 MeV ^{32}S bombardment are shown in Fig. 11, for fission fragments and for elastic scattering. The full lines represent calculations of blocking

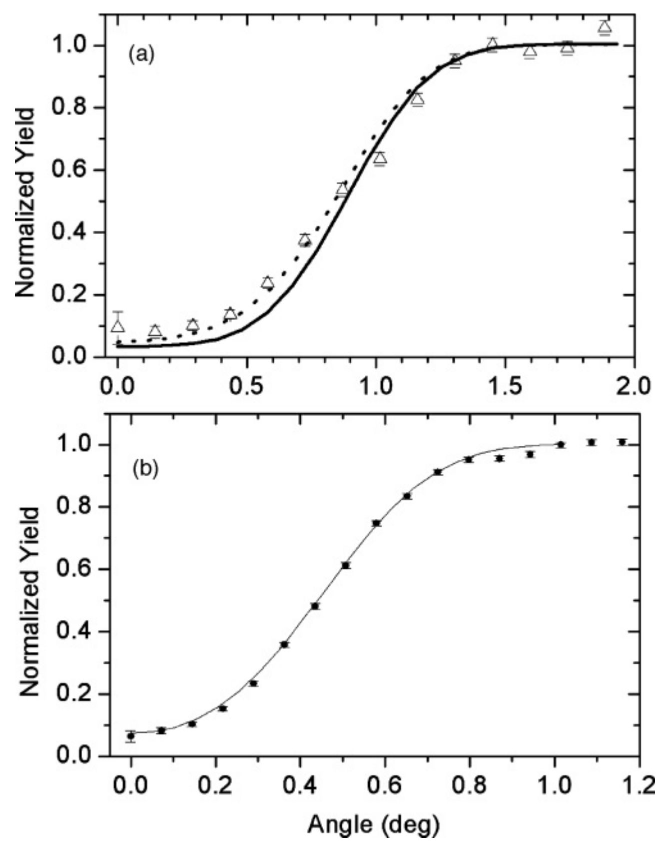

FIG. 11. Blocking dips for 180 MeV ^{32}S on W, (a) fission and (b) elastic scattering. The curves are calculations discussed in the text. The full drawn curves correspond to no recoil displacement and the dotted curve is a superposition of 75% without displacement and 25% with an exponential distribution of displacements with average $v\tau = 12$ pm.

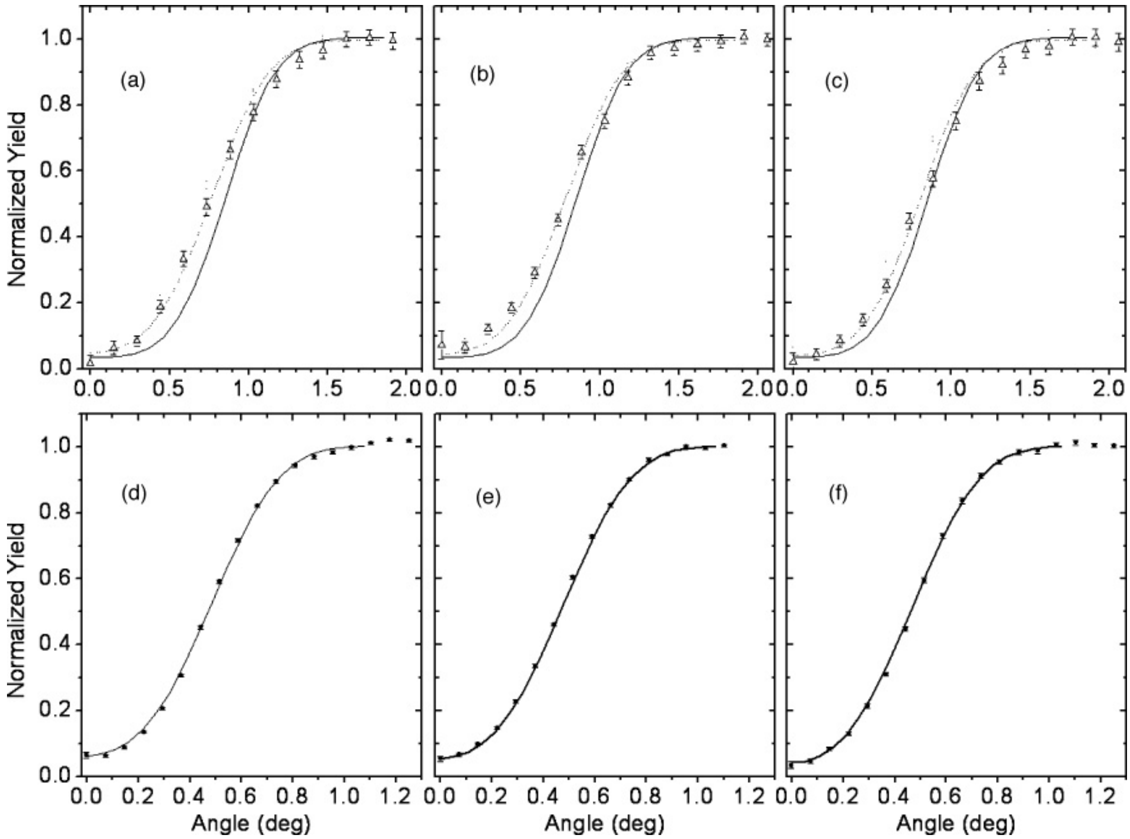

FIG. 12. Blocking dips in fission and elastic scattering for 240 MeV (a,d), 245 MeV (b,e), and 255 MeV (c,f) ^{48}Ti, compared with calculations. The full drawn curves correspond to no recoil displacement while the dotted curves include exponential distributions of displacements from the ⟨111⟩ row, with average values (a) 6 pm, (b) 5 pm, and (c) 4 pm.

dips without any recoil displacement. The calculations were discussed in Sec. IV. The two parameters adjusted to fit the dip for elastics are the Gaussian mosaic spread of the crystals with 0.35 deg FWHM and a small 'random' component (3%). These parameters were kept fixed in all calculations and give excellent agreement with all blocking dips for elastic

TABLE I. Summary of the results. The energies are given in MeV, the cross sections in mb, the distances in pm, and the times in as.

Ion	E_{lab}	E^{*} [b]	B_{lab} [c]	$\langle E_f \rangle_{\text{th}}$ [d]	$\langle E_f \rangle_{\text{exp}}$ [e]	$\sigma_{f,\text{calc}}$	$\sigma_{f,\text{exp}}$	$v\tau$	τ
^{32}S [a]	180	72.1	157.1	116.6	120.0	361	337	12 [h]	3 [h]
^{48}Ti	240	49.9	224.8	135.8	139.1	199	224	6	1.2
^{48}Ti	245	53.9	224.8	136.0	139.1	260	278	5	1.0
^{48}Ti	255	61.8	224.8	136.5	139.0	373	408	4	0.7
^{58}Ni	330	64.0	294.3	154.6	164.9	357	299f	8	1.2
^{58}Ni	350	79.2	294.3	155.1	165.4	526	438 [f]	9	1.4
^{58}Ni	375	98.2	294.3	155.6	164.9	711	477 [f]	8	1.2
^{58}Ni [a]	350	79.2	294.3	155.1	157.0	526	438	8	1.2
^{74}Ge [a]	390	52.1	349.8	165.1	178.1	361	234 [g]	12	1.6

[a] Measured with 50 nm W crystal.
[b] Excitation energy calculated with atomic masses from [42].
[c] Barrier energy from [43].
[d] Average kinetic energy of single fragment in the lab at 54.3° to the beam, from [41].
[e] Average over polygon, as illustrated in Figs. 2 and 10.
[f] Scaled to give the same cross section for 350 MeV as obtained with the wider polygon used for analysis of the second measurement at this energy.
[g] With narrow polygon.
[h] For 25% of the fissions (75% below ≈ 1 as).

scattering. The width of the blocking dip for fission fragments is fairly well reproduced by the calculation but there is a significant filling-in of the dip at angles just below the half width. This may indicate the presence of a small component of fissions with a displacement of more than 10 pm, as illustrated by the dotted curve for 75% with zero displacement and 25% with an exponential distribution of displacements with average value12 pm.

The blocking dips for the ^{48}Ti measurements are illustrated in Fig. 12. The fission dips are seen to be narrower than the calculated dips without recoil displacement but the difference decreases with increasing bombarding energy. Good fits are obtained with exponential recoil distributions. As a test of the scaling with E and Z for fission fragments, we have split the polygon for fissions (Fig. 2(b)) into high- and low-energy parts, and the corresponding energy spectra are shown in upper part of Fig. 13. From the fission kinematics and the energy spectra we have calculated the ratio 0.84 of the average blocking widths for the two regions and a comparison of the blocking dips scaled with this ratio is shown in the lower part of Fig. 13. Within the statistical uncertainty the two dips agree.

The data obtained with Ni bombardment of the thicker crystal are shown in Fig. 14. There is an even more pronounced effect of recoil displacement on the fission dips, and all dips are fitted well with an exponential distribution of recoils with an average about 8 pm. Note, that the fitted curves should be somewhat lower than the measured ones at the smallest angles due to the Barrett effect discussed in Sec. IV. The measurement at 350 MeV was repeated with the thinner crystal in the third experiment and the fission dip is shown in Fig. 15(b). For this measurement, illustrated in Fig. 2(c), we have also set a polygon on deep inelastic scattering in the region just left of the elastic peak. The corresponding blocking dip is shown in Fig. 15(a). Apart from a 10% increase in minimum yield, which might be due to a contribution from scattering in the crystal backing (Mo), this dip is in good agreement with a calculation without recoil displacement.

Finally, the data obtained for bombardment with 390 MeV ^{74}Ge are shown in Fig. 16. The statistics are poor for fissions but sufficient to reveal a fairly large recoil displacement. Note also the good agreement with the calculation for the dip in elastic scattering, confirming the simple scaling of the width with Z_1 and E in Eq. (4.2), without any correction for screening by projectile electrons of the Coulomb interaction with crystal atoms, as discussed in Sec. IV.

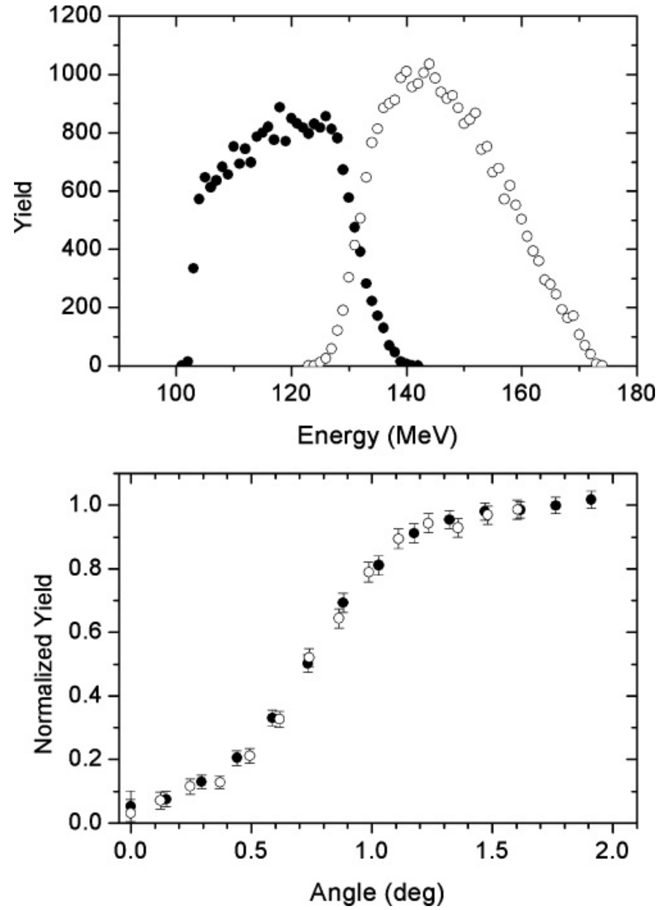

FIG. 13. Analysis of fission for 245 MeV ^{48}Ti bombardment with two polygons, containing high- and low-energy fragments, respectively. The energy spectra are shown in the upper figure and the corresponding blocking dips below with the same symbols. A scale factor of 0.84, calculated from the fission kinematics with a fixed fragment charge-to-mass ratio, has been applied to the angles at the lower energies.

VI. DISCUSSION

The parameters for the reactions studied and the results of the analysis are summarized in Table I. Fission from reactions with W nuclei has been identified in the 2D-plots illustrated in Fig. 2 and has been confirmed by the good agreement of the energy spectra with theory shown in Fig. 10. A further confirmation is provided by the comparison of the measured and calculated fission cross sections in the table. The experimental cross sections have been obtained from the Rutherford cross section for elastic scattering combined with the measured ratio between fission and elastic events. The calculated cross sections have been obtained from the simple estimate

$$\sigma_{f,\mathrm{calc}} = (1-k)\pi r_0^2\left(A_1^{1/3}+A_2^{1/3}\right)^2(1-B/E). \quad (6.1)$$

We have used $r_0 = 1.2$ fm and a simple form of the Bass barrier [43], given in the center-of-mass system by

$$B_{\mathrm{C.M.}} = 1.438\,(\mathrm{MeV})\,Z_1Z_2\big/\left[1.07\left(A_1^{1/3}+A_2^{1/3}\right)+2.7\right] - 2.9A_1^{1/3}A_2^{1/3}\big/\left(A_1^{1/3}+A_2^{1/3}\right). \quad (6.2)$$

The leading factor in Eq. (6.1) accounts for a reduction corresponding to deep inelastic scattering and we have used $k = 0.2$. We have also made an average over a Gaussian distribution of barrier heights with 6 MeV standard deviation but at our bombarding energies the effect on the cross section is negligible. For S and Ti the cross sections agree within about 10% but there are larger deviations for the heavier projectiles. We have not made any correction for the cuts in fission energy, except for the renormalization of the Ni data. As seen from

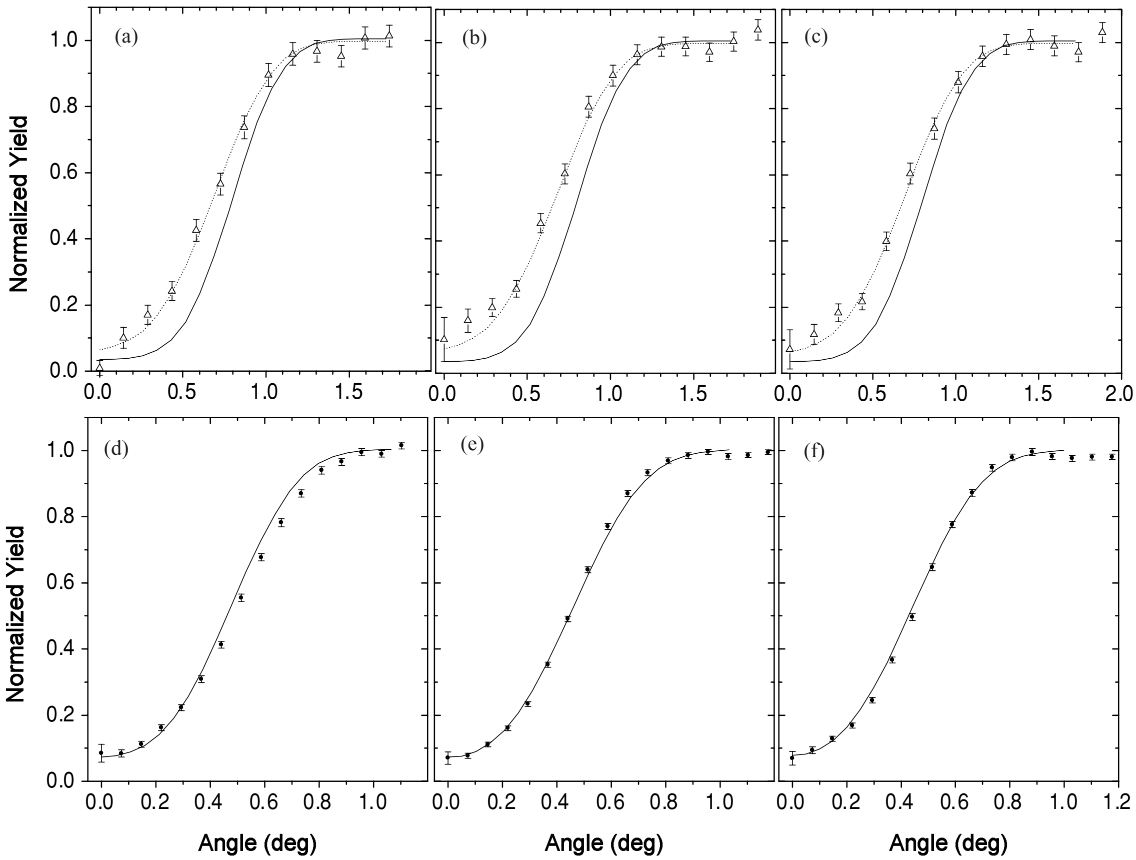

FIG. 14. Blocking dips in fission and elastic scattering for 330 MeV (a,d), 350 MeV (b,e), and 375 MeV (c,f) ^{58}Ni, compared with calculations. The dotted curves include exponential distributions of recoil displacements from the ⟨111⟩ row, with average values (a) 8 pm, (b) 9 pm, and (c) 8 pm.

Fig. 10, the polygon cut does not reduce the cross section much for the lighter projectiles but for Ge there is a large reduction.

The delay in the fission process is derived from an analysis of the blocking patterns generated by the interaction of the fission fragments with the thin tungsten target crystals. The ⟨111⟩ axial blocking dips are compared with those for elastic scattering, and the observed differences are interpreted as results of recoil distances of order 10 pm in the fission reactions. For such small recoil distances, the main influence on the blocking dips is a narrowing, and the analysis requires an accurate angular calibration of the detector.

For elastic scattering, the calibration can be derived directly from measurements with a mask in front of the counter. However, it was too time consuming to record mask spectra with fission fragments and instead the calibration for the simultaneously recorded elastic scattering was applied as in earlier work [24,25]. We found in the present analysis that one then must correct for the different depth profiles of energy deposition in the counter. Fortunately, this correction can be determined quite accurately and, as the correction for mosaic spread, it has been tested by measurements of elastic scattering at different bombarding energies. In a short publication of some of the present data [25], the correction for different depth profiles of energy loss was not included and this accounts for the differences of nearly a factor of two between the delays derived from the measurements there and here.

An important tool in the analysis is calculation of the dip shape. The model calculations reproduce very accurately the blocking dips for elastic scattering with an important correction for mosaic structure of the thin crystals. Mosaic structure introduces an absolute angle, the width of the Gaussian distribution of orientations of the microcrystals, and thereby breaks the simple scaling of the blocking angles with the square root of the Z_1/E ratio. We have confirmed this correction by measurements of elastic scattering at different bombarding energies. In the first measurement for ^{32}S on W [24] neither of the two corrections was applied and it was concluded that there was not a significant lifetime effect on the blocking. Including the two corrections, we find here a significant lifetime effect but the corrections partly cancel and the lifetime effect is small for ^{32}S bombardment.

The great strength of the crystal blocking method for lifetime determination is that it is a direct time-of-flight technique which does not rely on assumptions about the nuclear dynamics like, for example, the ‘neutron clock.’ The results have strong implications for the dynamics of heavy-ion induced fission. Except for the lightest projectile, ^{32}S, our results are consistent with exponential distributions of delays with a single lifetime of order 1 as. This is in

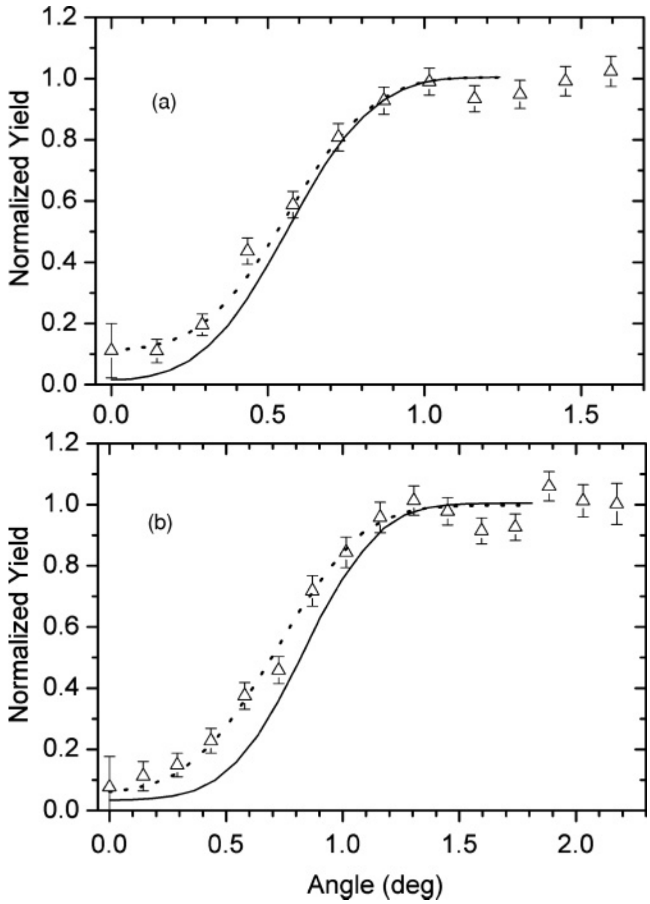

FIG. 15. (a) Blocking for deep inelastic scattering of 350 MeV ^{58}Ni on W (third experiment), compared with a calculation including a 10% random component (dotted curve). The average energy is about 80 MeV lower than for elastic scattering. (b) Fission blocking for 350 MeV ^{58}Ni on W (third experiment) compared with calculations. The dotted curve includes an exponential distribution of recoil displacements from the ⟨111⟩ row with average value 8 pm.

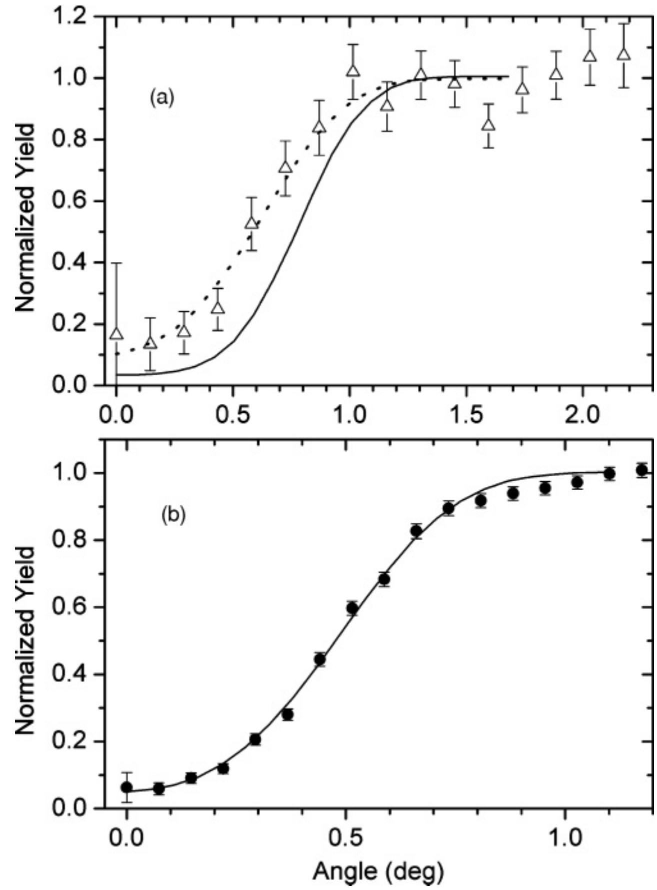

FIG. 16. Blocking dips in fission (a) and elastic scattering (b) for 390 MeV ^{74}Ge on W compared with calculations. The dotted curve includes an exponential distribution of recoil displacements from the ⟨111⟩ row with average value 12 pm.

strong contradiction to the prediction of the Bohr-Wheeler model of a compound nucleus in statistical equilibrium, with a competition between fission and neutron emission which results in multichance fission and a broad distribution of lifetimes. Instead the results support the picture of heavy-ion induced fission as mainly quasi-fission without formation of a compound nucleus [21,22]. The long lifetime is then a consequence of strong damping of the dynamics of deformation of the mononucleus and not of confinement by a fission barrier.

There is strong independent experimental evidence supporting the picture of mainly quasifission in heavy-ion induced reactions [26–28]. Of particular relevance to our measurements is the comparison in [27] of different reactions forming ^{220}Th. It was shown that for heavy projectiles (^{40}Ar, ^{48}Ca, ^{82}Se, and ^{124}Sn) the cross section for xn evaporation residue formation is typically an order of magnitude lower than for ^{16}O. In our measurements of ^{32}S induced fission we also form thorium isotopes, with mass numbers 214–216 and 218. The projectile is in the transition region between ^{16}O and ^{40}Ar, closer to the latter. It is interesting that this is the only case where a two component fit is required to reproduce the measured fission blocking dip. Perhaps the small component with about 3 as delay can be associated with CN formation while the larger fast component with delay shorter than 1 as is from quasifission.

As stressed in [21], the picture of quasi-fission also explains the weak dependence of the fission time scale on fissility. However, the delay times measured here are about two orders of magnitude longer than obtained there for systems expected to be dominated by quasifission. A possible explanation for this large discrepancy is suggested by the alternative analysis of neutron measurements in [22]. More excitation energy is tied up in potential energy in quasifission than in the compound nucleus and hence neutron emission is slower. The delays derived in [22] from neutron data are typically a few tenths of an attosecond, somewhat shorter than our findings. However, we have studied reaction systems at energies rather close to the fission threshold, and the delay times could be shorter at higher bombarding energies. We find a significant energy dependence for ^{48}Ti induced fission but no systematic variation in a much broader energy interval for ^{58}Ni bombardment.

To investigate whether a picture of quasi-fission with strongly damped dynamics may be consistent with our experimental results we discuss below estimates of delay times obtained from a simple diffusion model with one-body viscosity. We find that indeed a time scale of order one attosecond is possible with a nearly exponential distribution of delay times. It is also possible that the blocking measurements for super-heavy composite nuclei can be understood from such a picture [13,14]. A filling-in of the fission blocking dips was observed, indicating an attosecond lifetime, but the shapes of the dips were not analyzed in detail so little can be concluded about the distribution of delay times.

VII. FISSION BY DIFFUSION

A diffusion model was used in [16,30,31] to estimate the probability for formation of a compound nucleus after the initial contact between two heavy nuclei. After a rapid neck formation, the system is located in an asymmetric-fission valley of the potential-energy surface. This is illustrated schematically in Fig. 17, showing the potential $V(x)$ as a function of the deformation x. For very high atomic numbers of the composite nucleus the initial configuration is less compact than at the fission barrier. In the simple one-dimensional picture in Fig. 17, the 'injection' point x_0 is therefore outside the fission barrier and formation of a compound nucleus (CN) requires uphill diffusion, across the fission barrier.

We are instead interested in the dynamics of the majority of the systems, moving towards larger deformations and eventual scission at $x = L$(quasifission).[1] For fissilities around 0.8 the liquid drop potential is very flat [21,22], and if the viscosity is high the dynamics may be described as diffusion [30]. The continuity equation for the probability distribution $W(t, x)$, expressing conservation of the total probability, may be written as

$$-\frac{\partial W}{\partial t} = -\mu \frac{\partial}{\partial x}\left(\frac{\partial V}{\partial x} W\right) - D\frac{\partial^2}{\partial x^2} W. \tag{7.1}$$

The right hand side is the divergence of the probability current, which is the sum of a drift current and a diffusion current, and the mobility μ and the diffusion constant D are assumed independent of x. They are connected by the Einstein-Smoluchowski relation between diffusion and dissipation, $D = \mu T$, where T is the temperature and the Boltzmann constant is set equal to unity. For a distribution completely confined by a potential, the time independent solution is the Boltzmann distribution, $W(x) \propto \exp(-V(x)/T)$. Without the first term on the right hand side, the drift term, the solution of Eq. (7.1) is a Gaussian with variance $\sigma^2 = 2Dt$.

If we replace $V(x)$ in Fig. 17 by a linear potential, corresponding to a constant driving force F, Eq. (7.1) has an analytical solution,

$$W(x,t) = \frac{1}{\sqrt{4\pi Dt}} \exp\left(-\frac{(x - x_0 - \mu F t)^2}{4Dt}\right), \tag{7.2}$$

for $W(x,0) = \delta(x–x_0)$. The drift term in Eq. (7.1) just gives a displacement of the Gaussian distribution function, with velocity μF. When the drift term dominates, the distribution moves towards L without much broadening and the characteristic decay time becomes $t = (L–x_0)/\mu F$. When the driving force is small the maximum remains near $x = x_0$. The delay may then be characterized by the time when the variance of the Gaussian becomes equal to $(L–x_0)^2$,

$$t_{\mathrm{diff}} = (L - x_0)^2/2D. \tag{7.3}$$

We replace the fission barrier by a perfectly reflecting wall at $x = x_0$. With a reduced time defined by $\tau = t/t_{\mathrm{diff}}$ the fraction of systems having undergone scission is then given by the complement to the error function,

$$S(\tau) = 1 - \mathrm{erf}(1/\sqrt{2\tau}), \tag{7.4}$$

and the decay rate is the derivative of this function, $I(\tau) = S'(\tau)$. As seen in Fig. 18, the rate grows from zero at $\tau = 0$ to a maximum near $\tau = 0.35$, and $I(\tau) = 0.7\exp(-\tau)$ is a fair approximation for τ of order unity. Asymptotically, $I(\tau)$ decreases as $\tau^{-3/2}$ but, as shown below, the decrease becomes exponential with an absorbing wall at $x = L$, representing scission.

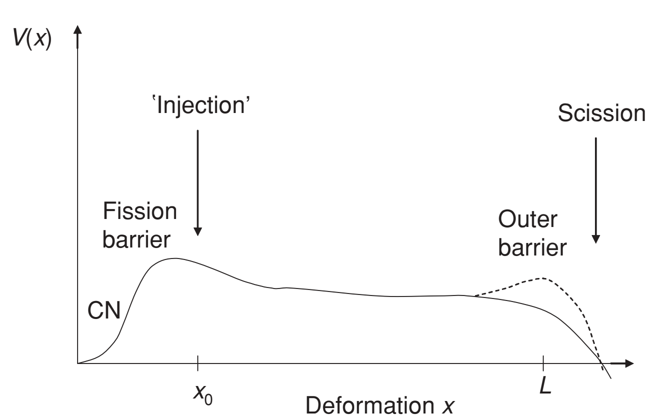

FIG. 17. Qualitative illustration of the potential energy of a composite nucleus as a function of deformation. The 'Injection' arrow indicates the deformation after touching of the two nuclei and neck formation.

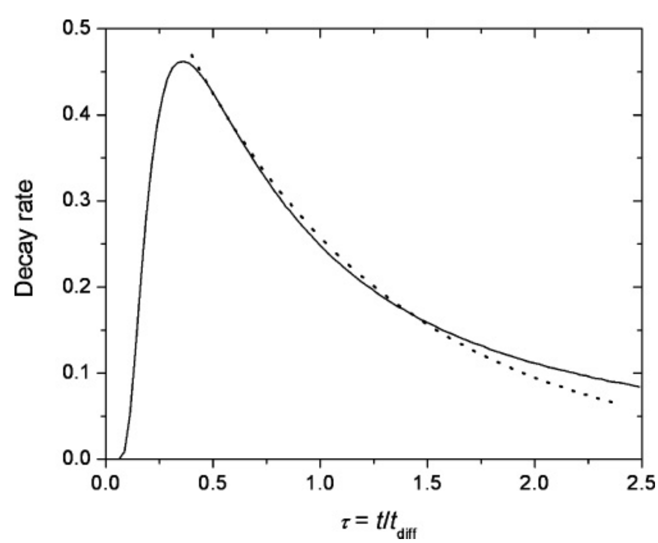

FIG. 18. Illustration of the function $I(\tau)$ defined below Eq. (7.4). The dotted curve is the approximation $I(\tau) \simeq 0.7\exp(I(\tau))$.

To estimate the diffusion time we need a simple estimate of the mobility μ. The mononucleus is represented by a cylinder with length $2x$ and radius r. Let x increase at a rate dx/dt with a corresponding decrease of r to preserve volume. We use the standard one-body dissipation formula [44–46] for the negative of the derivative of the energy with respect to x, the force resisting the deformation. The force is written as an integral over the surface of the nucleus,

$$F = \rho \langle p \rangle \oint \frac{dn}{dt}\frac{dn}{dx} d\sigma, \tag{7.5}$$

where $d\sigma$ is the differential area, dn is the normal displacement of the surface induced by the change dx, ρ is the nuclear number density and $\langle p \rangle$ the mean magnitude of the nucleon momentum, equal to 3/4 of the Fermi momentum p_F. The right hand side is proportional to the deformation speed (dx/dt). Solving for this speed and writing it as μF, we obtain the following expression:

$$\mu(x)^{-1} = \rho \langle p \rangle (\text{Volume}/x)(1 + r/2x). \tag{7.6}$$

The neutrons and protons are treated as independent Fermi gases, each with half the nucleons, $Z = N = A/2$. The result is insensitive to the difference between Z and N. The Fermi momentum is then given by $p_F = (3\pi^2/2)^{1/3}\hbar\rho^{1/3}$.

Introducing the radius constant r_0 through $\rho = 1/(4\pi/3)r_0^3$, we obtain for the product $\rho\langle p \rangle$ in Eq. (7.6)

$$\rho \langle p \rangle = \frac{27}{32\pi}\left(\frac{\pi}{3}\right)^{1/3}\frac{\hbar}{r_0^4}. \tag{7.7}$$

With the simplifying assumption that μ remains constant at its value at injection, the characteristic diffusion time is given by Eq. (7.3) and the Einstein-Smoluchowski relation. We write the initial value of x as $x_0 = R_0\alpha$ and $L - x_0 = R_0\beta$, where R_0 is the equivalent sharp radius, $R_0 = A^{1/3}r_0$. The final formula for the diffusion time then becomes

$$t_{\text{diff}} = 3.76 \cdot 10^{-4}\frac{A^{4/3}}{T}\frac{\beta^2}{\alpha}\left(1 + \frac{1}{\sqrt{6\alpha^3}}\right), \tag{7.8}$$

where time is measured in attoseconds and temperature in MeV. With $T = 1$ MeV and $\alpha = 1.5$ inside the brackets this gives for $A = 232$

$$t_{\text{diff}} = 0.65\,\frac{\beta^2}{\alpha}. \tag{7.9}$$

This is a remarkable result. A simple diffusion calculation with a diffusion constant corresponding to one-body dissipation gives a lifetime not too far from our observations! The delay time is somewhat shorter when the x dependence of the mobility is included and inclusion of neck formation will lead to a further reduction of the damping and of the delay time. Conversely, the presence of a low outer fission barrier could increase the delay, as discussed below.

A. Puddle of stability

Let us try to estimate the influence of a lower outer barrier on the diffusion (dashed curve in Fig. 17). This barrier could come from a combination of the liquid drop potential with shell effects. Shell effects give a minimum of the potential energy around a 2:1 deformation ratio, forming perhaps a shallow 'puddle of stability.' The inner fission barrier is larger for the systems studied here and is most important for CN fission but there is also an outer barrier of a few MeV ([32], p. 888).

The following considerations are at first based on a perturbation approach. The distribution $W(x,t)$ is assumed to be determined by diffusion in a flat potential and we then estimate the modification of the diffusion current by a shallow potential minimum. A simple model potential is $V(x) = {}^1/_2 bx^2$. The injection point in Fig. 17 now corresponds to $x = 0$, and we imagine that the fission barrier is a reflecting wall so we can solve the diffusion equation for a symmetric x interval. We assume that at $x = \pm L$ there are perfectly absorbing walls so the maximum of the potential is $V_{\max} = {}^1/_2 bL^2$. The condition for the potential not to play a significant role for the diffusion is that the drift current is small compared with the diffusion current. The ratio of the diffusion current to the drift current at x is

$$-D\frac{\partial}{\partial x}W/\mu bxW = -(D/\mu bx)\frac{\partial}{\partial x}\ln W = D/\mu b\sigma^2, \tag{7.10}$$

where σ^2 is the variance of the Gaussian. We use the relation $D = \mu T$ and insert $\sigma^2 = L^2/2$ to obtain a rough estimate of the relative importance of diffusion and drift,

$$\text{diffusion/drift} \approx 2T/bL^2 = T/V_{\max}. \tag{7.11}$$

This is a very simple result: the energy fluctuations in the system are of order T, and the barrier before scission has to be larger than T to be important. The implication is that even a barrier of order 1 MeV will slow down the diffusion significantly (a very similar result was derived in [30]).

To make a numerical simulation we introduce reduced variables. The natural variables are $\xi = x/L$ and $\tau = t/t_{\text{diff}}$, with $x_0 = 0$ in Eq. (7.3). The diffusion equation then becomes

$$-\frac{\partial W}{\partial \tau} = -\frac{1}{2T}\frac{\partial}{\partial \xi}\left(\frac{\partial V}{\partial \xi}W\right) - \frac{1}{2}\frac{\partial^2}{\partial \xi^2}W, \tag{7.12}$$

with the boundary condition that $W(\xi)$ vanish at $\xi = \pm 1$. The maximum of the barrier is denoted $V_{\max} = \gamma T$ and with the harmonic potential we then obtain

$$-\frac{\partial W}{\partial \tau} = -\gamma\frac{\partial}{\partial \xi}(\xi W) - \frac{1}{2}\frac{\partial^2}{\partial \xi^2}W. \tag{7.13}$$

The survival as a function of time is shown in Fig. 19 for different values of γ. Without the potential, the probability of survival is about one third at t_{diff}. This stage of the decay is delayed by a factor of 2.4 for $\gamma = 2$.

As seen in the figure, the decay becomes exponential after some delay, and this can be understood from an expansion of W in eigenfunctions. For $V = 0$ the eigenfunctions of the differential operator on the right hand side of Eq. (7.12) are $\cos((n - 1/2)\pi\xi)$ and $\sin(n\pi\xi)$, and the lowest eigenvalue is $E_0 = \pi^2/8$. The corresponding term in the expansion dominates at long times, giving an exponential decay with decay constant E_0.

This result is more general. With a simple transformation of Eq. (7.12) we can make contact with a well known theorem in quantum mechanics. Multiplying by $\exp(V/2T)$ we find an

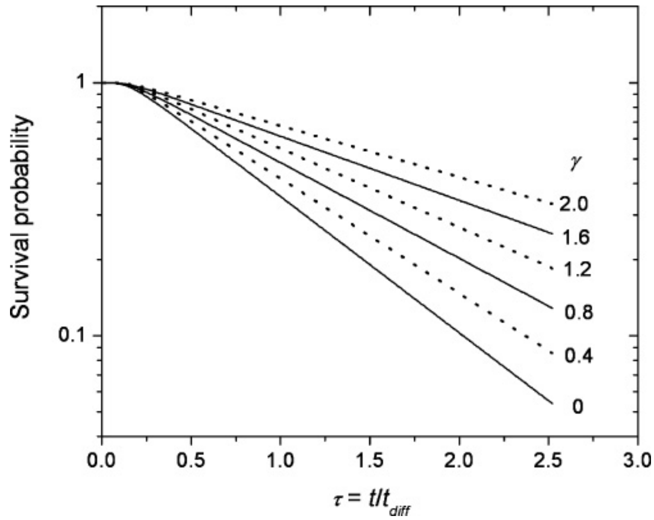

FIG. 19. Survival probability as a function of time for different values of the parameter γ in Eq. (7.13).

equation for the time derivative of $Y = \exp(V/2T)W$ with a differential operator which can be viewed as a Hamiltonian ($\hbar = m = 1$) with the potential $(V')^2/4T^2 - V''/4T$. With the boundary conditions that $Y(\xi, \tau)$ vanish at $\xi = \pm 1$, the Hamiltonian has discrete eigenvalues. The corresponding eigenfunctions form a complete set, and the solution to the equation for $Y(\xi, \tau = 0) = \delta(\xi)$ can be expanded in these functions. Again the term corresponding to the lowest eigenvalue, E_0, dominates at long times, and the decay becomes exponential with decay constant E_0.

The termination of the fission process by irreversible scission gives a similar boundary condition, and more realistic stochastic calculations may be expected also to give nearly exponential decay. However, the path to fission depends on the impact parameters in the reaction and the time distribution may be modified by the average over angular momentum (see the discussion in [22]).

VIII. SUMMARY AND CONCLUSIONS

We have carried out crystal blocking experiments for fission induced by bombardment of thin W crystals with 180 MeV ^{32}S, 240, 245, and 255 MeV ^{48}Ti, 330, 350, and 375 MeV ^{58}Ni, and 390 MeV ^{74}Ge ions. In earlier experiments with fission induced by lighter ions [2–7] an increase in the minimum yield in the blocking dips for fission fragments without a change in the width was observed, indicating the presence of a long-lived component. This component was identified as late-chance fission after evaporation of several neutrons [6]. In contrast, we have here observed a narrowing of the blocking dips for fission fragments with only a small increase in the minimum yield, and in nearly all cases the dips are consistent with exponential decay with a single lifetime of order 1 as. This is longer by orders of magnitude than expected for first chance fission.

The results are inconsistent with multi-chance fission of a Bohr compound nucleus in statistical equilibrium at each stage. There is independent strong evidence for dominance of quasifission without formation of a compound nucleus in heavy-ion induced fission [26–28], and the deformation dynamics may be pictured as strongly damped stochastic motion in a nearly flat potential [22]. We have made simple model calculations based on a diffusion equation with one-body dissipation. The model predicts nearly exponential decay and the estimated delays are of order attoseconds, consistent with the observations. We find that the presence of even a low outer fission barrier may contribute significantly to the delay [32].

Our results support the reinterpretation in [22] of data on pre-scission neutron emission and establish a new paradigm for analysis of heavy-ion induced fission. Also the interpretation of earlier crystal-blocking measurements of fission lifetimes in such reactions in terms of multichance fission of a Bohr compound nucleus may have to be revised [11–14]. In a very recent crystal-blocking experiment on fission in ^{208}Pb+Ge and ^{238}U+Ni reactions, the measurements were reproduced by simulations with exponential decay with lifetimes of 1 as and 2.2 as, respectively, for the fused nuclei with $Z = 114$ and $Z = 120$ [47]. Despite claims to the contrary, this is consistent with our results and supports our interpretation.

ACKNOWLEDGMENTS

We thank the HRIBF operations staff for providing the high quality, stable beams required for these experiments. We are grateful to W. J. Swiatecki for his continued interest in our results and for sharing with us his deep insight into the dynamics of heavy nuclei. Support by NATO Grant No. CLG980118 has been crucial for bringing together the international research group for experiments and data analysis. Research at the Oak Ridge National Laboratory was supported by the US Department of Energy under Contract No. DE-AC05-00OR22725 with UT-Batelle, LLC.

[1] W. M. Gibson, Annu. Rev. Nucl. Sci. **25**, 465 (1975).
[2] S. A. Karamian, Yu. Ts. Oganessian, and F. Normuratov, Yad. Fiz. **14**, 499 (1971) [Sov. J. Nucl. Phys. **14**, 279 (1972)].
[3] V. V. Kamanin, S. A. Karamian, F. Normuratov, and S. P. Tretyakova, Yad. Fiz. **16**, 447 (1972) [Sov. J. Nucl. Phys. **16**, 249 (1973)].
[4] V. N. Bugrov and S. A. Karamian, Yad. Fiz. **40**, 857 (1984) [Sov. J. Nucl. Phys. **40**, 546 1984].
[5] J. U. Andersen, E. Lægsgaard, K. O. Nielsen, W. M. Gibson, J. S. Forster, I. V. Mitchell, and D. Ward, Phys. Rev. Lett. **36**, 1539 (1976).
[6] J. U. Andersen, A. S. Jensen, K. Jørgensen, E. Laegsgaard, K. O. Nielsen, J. S. Forster, I. V. Mitchell, D. Ward, W. M. Gibson, and J. J. Cuomo, K. Dan. Vidensk Selsk. Mat. Fys. Medd. **40**, No. 7 (1980); http://www.sdu.dk/Bibliotek/matfys.

[7] J. S. Forster, I. V. Mitchell, J. U. Andersen, A. S. Jensen, E. Laegsgaard, W. M. Gibson, and K. Reichelt, Nucl. Phys. **A464**, 497 (1987).

[8] N. Bohr and J. A. Wheeler, Phys. Rev. **56**, 426 (1939).

[9] J. U. Andersen, N. G. Chechenin, A. S. Jensen, K. Jørgensen, and E. Lægsgaard, Nucl. Phys. **A324**, 39 (1979).

[10] J. D. Molitoris, W. E. Meyerhof, Ch. Stoller, R. Anholt, D. W. Spooner, L. G. Moretto, L. G. Sobotka, R. J. McDonald, G. J. Wozniak, M. A. McMahan, L. Blumenfeld, N. Colonna, M. Nessi, and E. Morenzoni, Phys. Rev. Lett. **70**, 537 (1993).

[11] F. Goldenbaum, M. Morjean, J. Galin, E. Liénard, B. Lott, Y. Périer, M. Chevallier, D. Dauvergne, R. Kirsch, J. C. Poizat, J. Remillieux, C. Cohen, A. L'Hoir, G. Prévot, D. Schmaus, J. Dural, M. Toulemonde, and D. Jacquet, Phys. Rev. Lett. **82**, 5012 (1999).

[12] F. Barrué, S. Basnary, A. Chbihi, M. Chevallier, C. Cohen, D. Dauvergne, H. Ellmer, J. Franckland, D. Jacquet, R. Kirsch, P. Lautesse, A. L'Hoir, M. Morjean, J. C. Poizat, C. Ray, and M. Toulemonde, Nucl. Instrum. Methods B **193**, 852 (2002).

[13] A. Drouart, J. L. Charvet, R. Dayras, L. Nalpas *et al.*, *International Symposium on Exotic Nuclei, Peterhof 2004* (World Scientific, Singapore, 2005), p. 192.

[14] M. Morjean, J. L. Charvet, A. Chbihi, M. Chevallier, C. Cohen, D. Dauvergne, R. Dayras, A. Drouart, J. D. Frankland, D. Jacquet, R. Kirsch, M. Laget, P. Lautesse, A. L'Hoir, A. Marchix, L. Nalpas, M. Parlog, C. Ray, C. Schmitt, C. Stodel, L. Tassan-Got, and A. Türler, Eur. Phys. J. D **45**, 27 (2007).

[15] S. Hoffmann, F. P. Hessberger, D. Ackermann, S. Antalic, P. Cagarda, B. Kindler, P. Kuusiniemi, M. Leino, B. Lommel, O. N. Malyshev, R. Mann, G. Muenzenberg, A. G. Popeko, S. Saro, B. Streicher, and A. V. Yeremin, Nucl. Phys. **A734**, 93 (2004).

[16] W. J. Swiatecki, K. Siwek-Wilczynska, and J. Wilczynski, Phys. Rev. C **71**, 014602 (2005).

[17] D. Hilscher and H. Rossner, Ann. Phys. (Paris) **17**, 471 (1992) and references therein.

[18] D. J. Hinde, D. Hilscher, H. Rossner, B. Gebauer, M. Lehmann, and M. Wilpert, Phys. Rev. C **45**, 1229 (1992).

[19] P. Paul and M. Thoennessen, Annu. Rev. Nucl. Part. Sci. **44**, 65 (1994).

[20] V. A. Rubchenya, A. V. Kuznetsov, W. H. Trzaska, D. N. Vakhtin, A. A. Alexandrov, I. D. Alkhazov, J. Äystö, S. V. Khlebnikov, V. G. Lyapin, O. I. Osetrov, Yu. E. Penionzhkevich, Yu. V. Pyatkov, and G. P. Tiourin, Phys. Rev. C **58**, 1587 (1998).

[21] D. J. Hinde, H. Ogata, M. Tanaka, T. Shimoda, N. Takahashi, A. Shinohara, S. Wakamatsu, K. Katori, and H. Okamura, Phys. Rev. C **39**, 2268 (1989).

[22] K. Siwek-Wilczinska, J. Wilczinski, R. H. Siemssen, and H. W. Wilscut, Phys. Rev. C **51**, 2054 (1995).

[23] J. P. Blocki, H. Feldmaier, and W. J. Swiatecki, Nucl. Phys. **A459**, 145 (1986).

[24] S. A. Karamian, J. S. Forster, J. U. Andersen, W. Assmann, C. Broude, J. Chevallier, J. S. Geiger, F. Grüner, V. A. Khodyrev, F. Malaguti, and A. Uguzzoni, Eur. Phys. J. A **17**, 49 (2003).

[25] J. U. Andersen, J. Chevallier, J. S. Forster, S. A. Karamian, C. R. Vane, J. R. Beene, A. Galindo-Uribarri, J. Gomez del Campo, H. F. Krause, E. Padilla-Rodal, D. Radford, C. Broude, F. Malaguti, and A. Uguzzoni, Phys. Rev. Lett. **99**, 162502 (2007).

[26] A. C. Berriman, D. J. Hinde, M. Dasgupta, C. R. Morton, R. D. Butt, and J. O. Newton, Nature **413**, 144 (2001).

[27] D. J. Hinde, M. Dasgupta, and A. Mukherjee, Phys. Rev. Lett. **89**, 282701 (2002).

[28] D. J. Hinde and M. Dasgupta, Phys. Lett. **B622**, 23 (2005).

[29] J. Töke, R. Bock, G. X. Dai, A. Gobbi, S. Gralla, K. D. Hildenbrand, J. Kuzminski, W. F. J. Müller, A. Olmi, H. Stelzer, B. B. Back, and S. Bjørnholm, Nucl. Phys. **A440**, 327 (1985).

[30] W. J. Swiatecki, K. Siwek-Wilczynska, and J. Wilczynski, Acta Phys. Pol. B **34**, 2049 (2003).

[31] K. Siwek-Wilczynska, I. Skwira-Chalot, and J. Wilczynski, Int. J. Mod. Phys. E **16**, 483 (2007).

[32] S. Bjørnholm and J. E. Lynn, Rev. Mod. Phys. **52**, 725 (1980).

[33] W. Assmann, H. Huber, C. Steinhausen, M. Dobler, H. Gluckler, and A. Weidinger, Nucl. Instrum. Methods Phys. Res. B **89**, 131 (1994).

[34] J. Lindhard, K. Dan. Vidensk. Selsk. Mat. Fys. Medd. **34**, No. 14 (1965); http://www.sdu.dk/Bibliotek/matfys.

[35] E. Fuschini, F. Malaguti, A. Uguzzoni, and E. Verondini, Radiat. Eff. **81**, 37 (1984).

[36] J. H. Barrett, Phys. Rev. B **3**, 1527 (1971).

[37] J. H. Barrett, Phys. Rev. Lett. **31**, 1542 (1973).

[38] J. U. Andersen and A. Uguzzoni, Nucl. Instrum. Methods Phys. Res. B **48**, 181 (1990).

[39] J. U. Andersen, B. Bech Nielsen, A. Uguzzoni, E. Fuschini, E. F. Kennedy, and V. A. Ryabov, Nucl. Instrum. Methods Phys. Res. B **90**, 166 (1994).

[40] S. Köster, Berichte der Kernforschungsanlage Jülich-Nr. 1799 (1982).

[41] V. E. Viola, K. Kwiatkowski, and M. Walker, Phys. Rev. C **31**, 1550 (1985).

[42] P. Moeller, J. R. Nix, W. D. Myers, and W. J. Swiatecki, At. Data Nucl. Data Tables **59**, 185 (1995).

[43] R. Bass, Nucl. Phys. **A231**, 45 (1974).

[44] J. Blocki, Y. Boneh, J. R. Nix, J. Randrup, M. Robel, A. J. Sierk, and W. J. Swiatecki, Ann. Phys. (NY) **113**, 330 (1978).

[45] J. Randrup and W. J. Swiatecki, Ann. Phys. **125**, 193 (1980).

[46] W. J. Swiatecki, Nucl. Phys. **A574**, 233c (1994).

[47] M. Morjean, D. Jacquet, J. L. Charvet, A. L'Hoir, M. Laget, M. Parlog, A. Chbihi, M. Chevallier, C. Cohen, D. Dauvergne, R. Dayras, A. Drouart, C. Escano-Rodriguez, J. D. Frankland, R. Kirsch, P. Lautesse, L. Nalpas, C. Ray, C. Schmitt, C. Stodel, L. Tassan-Got, E. Testa, and C. Volant, Phys. Rev. Lett. **101**, 072701 (2008).